Available online at www.sciencedirect.com

SCIENCE DIRECT®

International Journal of Heat and Mass Transfer 47 (2004) 4165–4175

International Journal of HEAT and MASS TRANSFER

www.elsevier.com/locate/ijhmt

Numerical modeling of scanning laser-induced melting, vaporization and resolidification in metals subjected to time-dependent heat flux inputs

Haseung Chung, Suman Das *

Department of Mechanical Engineering, The University of Michigan, 2250 GG Brown, 2350 Hayward Street, Ann Arbor, MI 48109-2125, USA

Received 20 March 2004; received in revised form 6 May 2004
Available online 2 July 2004

Abstract

We present a 1-D heat transfer, melting, vaporization and resolidification model describing the interaction of a scanning continuous-wave laser with a metal surface wherein the beam power is rapidly time-varying. The effects of processing parameters on process variables for linear ramp and quadratic heat flux inputs are investigated numerically by varying beam diameters, scan speeds and substrate temperatures. Relations are derived for the times to initiate melting, to initiate vaporization, to reach maximum melting depth, for melting–resolidification, and for maximum melting and vaporization depths. Surface temperatures for both heat flux inputs are compared with approximate closed form solutions.

Keywords: Laser processing; Melting; Vaporization; Resolidification; Stefan problem

1. Introduction

Direct selective laser sintering (SLS) of metals is a complex process exhibiting multiple modes of heat, mass and momentum transfer, and chemical reaction mechanisms. The inherent complexity of this process requires the construction of increasingly sophisticated models to enable a fundamental understanding of the important physical mechanisms. To understand and control this process, the temperature distribution inside the material and the melt depth information needs to be known as a function of time-varying processing parameters including the input laser power, beam diameter and scanning speed. In order to implement real-time control for laser power, beam diameter, and scan speed, an understanding of the response of melting, vaporization and resolidification processes to time dependent heat flux input is essential. This is especially necessary to account for process perturbations that occur due to deliberate or random fluctuations in laser power, due to different boundary conditions where a layer of powder has a previously solidified layer surface underneath (conducting) vs. powder underneath (relatively insulating), as well as to account for variations in thermophysical, optical and material properties when multiple materials are used to make heterogeneous parts. In a previous article [2], we presented a one-dimensional model that describes the physical mechanisms of heat transfer, melting, vaporization and resolidification taking place during and after the interaction of a laser beam with semi-infinite crystalline surface was developed. Results of numerical modeling for a step heat flux input were obtained. In this article, we extend the analysis to time-varying heat flux inputs, specifically time-dependent, linearly and quadratically increasing heat flux inputs. Although our intent is to understand such phenomena occurring in SLS where a laser beam interacts with a

* Corresponding author. Tel.: +1-734-615-6646; fax: +1-734-647-3170.
E-mail address: sumandas@umich.edu (S. Das).

0017-9310/$ - see front matter © 2004 Elsevier Ltd. All rights reserved.
doi:10.1016/j.ijheatmasstransfer.2004.05.009

Nomenclature

B_f	boundary heat flux factor
d	beam diameter
Fo	Fourier number $(=\frac{\alpha_s t}{r^2})$
L	domain length
P	laser power
Q_r	supplied total energy density$(=\frac{2P}{\pi dv}$, linear ramp heat flux input)
Q_q	supplied total energy density$(=\frac{4P}{3\pi dv}$, quadratic heat flux input)
q''	laser heat flux
$\dot{q}$	heat flux input rate
r	beam radius
t_i	time to initiate melting
t_{vi}	time to initiate vaporization
t_{max}	time to reach maximum melt depth
t_{tot}	total melting–resolidification time
v	beam scan speed
$x_{f,max}$	maximum melt depth
$x_{vf,max}$	maximum vaporization depth

Greek symbols

α_a	optical absorptivity
α	thermal diffusivity
ζ_{max}	dimensionless maximum melting depth
$\zeta_{v,max}$	dimensionless maximum vaporization depth
θ_i	dimensionless initial temperature
θ_s	dimensionless surface temperature
λ	latent heat of fusion
ρ	material density
τ	beam material interaction time
τ_i	dimensionless time to initiate melting
τ_{vi}	dimensionless time to initiate vaporization
τ_{int}	dimensionless beam material interaction time
τ_{max}	dimensionless time to reach maximum melting depth
τ_{tot}	dimensionless time for melting and resolidification
ϕ	dimensionless absorbed laser energy density

Subscripts

s	solid
f	solid–liquid interface
vf	liquid–vapor interface

metal powder bed, the model developed here is applicable in general to laser melting of metals, provided the 1-D assumption is met and boundary conditions are satisfied. A dimensionless analysis of the controlling parameters under various conditions is conducted.

2. Model description and numerical scheme

Understanding and predicting melting, vaporization and resolidification as a function of time-varying heat flux input is important for real-time control of laser fusion based manufacturing processes. Furthermore, dimensionless analyses of scaling laws relating process variables to controllable process parameters in such processes are especially useful in understanding process dynamics. In the future these laws can be incorporated into solidification models that can predict microstructure formation as a function of processing parameters. In a previous article [2], we presented a 1-D physical model in dimensionless form and a numerical scheme for solving the resulting equations. To summarize briefly, the following assumptions were made for developing the model. First, powder is treated as a solid and no sintering densification occurs during the process. Laser beam intensity distribution is assumed uniform across the beam diameter and constant material properties are assumed for each phase. Convective heat transfer at the top surface is neglected. The process is assumed to occur in an inert atmosphere at 1 atm ambient pressure [3]. Further, the vaporization temperature is assumed to be equal to the saturation temperature at ambient pressure. Melt pool convection and convective heat transfer at melt interface are also neglected. The melt interface is considered to propagate in planar shape and the top surface is assumed to be diffuse and gray. In order to satisfy the 1-D approximation, the beam–material interaction time, defined as the time taken by the beam to traverse one beam diameter, is small compared to the radial thermal diffusion time. We also developed a front tracking scheme with fixed grid and fixed time step based on a finite volume method [4]. An explicit discretization scheme satisfying stability criteria was employed to solve the equations. The accuracy of this method was verified via comparison with closed form solutions for surface temperature as a function of time [5].

As before, we define t_i as the time to initiate melting, t_{vi} the time to initiate vaporization, t_{max} the time to reach maximum melt depth, t_{tot} the total melting–resolidification time, $x_{f,max}$ the maximum melt depth, $x_{vf,max}$ the maximum vaporization depth. Here, the absorbed laser energy densities are $\frac{\alpha_a q'' t}{2}$ for ramp heat flux input and $\frac{\alpha_a q'' t}{3}$ for quadratic heat flux input. Their dimensionless counterparts are $\tau_i = \frac{\alpha_s t_i}{L^2}$, $\tau_{vi} = \frac{\alpha_s t_{vi}}{L^2}$, $\tau_{max} = \frac{\alpha_s t_{max}}{L^2}$, $\tau_{tot} = \frac{\alpha_s t_{tot}}{L^2}$, $\zeta_{max} = \frac{x_{f,max}}{L}$, $\zeta_{v,max} = \frac{x_{vf,max}}{L}$, $\phi = B_f \cdot \frac{1}{2} \cdot \frac{d/v}{d^2/4\alpha_s} = \frac{\alpha_a q''}{\rho v \lambda}$ (for ramp heat flux input) and $\phi = B_f \cdot \frac{1}{3} \cdot \frac{d/v}{d^2/4\alpha_s} = \frac{2\alpha_a q''}{3\rho v \lambda}$ (for quadratic heat flux input).

3. Simulation parameters

Numerical computations were conducted for two types of time-dependent laser heat flux input; ramp heat flux input (laser power linearly ramps from zero to full power during beam–material interaction time, followed by a drop to zero power), quadratic heat flux input (laser power increases quadratically from zero to full power during beam–material interaction time, followed by a drop to zero power). The concept of beam–material interaction time is used to simulate the temporal action of a moving laser beam over a surface area corresponding to one beam diameter, and can be used to set the duration for heat flux input experienced by an area of the surface corresponding to one beam diameter. Computations were carried out for 10 different beam diameters with 4 different scan speeds. Therefore, each type of heat flux input was investigated for 40 different beam–material interaction times. In order to investigate the effect of substrate preheat temperature, five different initial temperatures were tested keeping beam diameter and scan speed fixed ($d = 200$ μm, $v = 1.0$ m/s). The material properties of Nickel were used for computations. Table 1 shows beam diameters and scan speeds selected for the computations, satisfying the one-dimensional approximation ($\tau_{int} = \frac{d}{v} / \frac{(d/2)^2}{\alpha_s} \ll 1$).

Other parameter values used for the computations are shown in Table 2.

4. Results and discussion

The computations yielded predictions of temperature history, interface location, and interface velocity as functions of time and processing parameters. Further, relations between dimensionless process variables τ_i, τ_{vi}, τ_{max}, τ_{tot}, ζ_{max}, $\zeta_{v,max}$ and controllable process parameters τ_{int} (determined by v and d), and dimensionless input laser energy density ϕ were developed. These relations are discussed below.

Table 2
Parameters used for numerical computations II

Domain size	Number of nodes	Time step	Laser beam power
5 mm	500	1×10^{-8}	1 kW

4.1. Linear ramp heat flux input

4.1.1. Time to initiate melting

Fig. 1(a) shows plots of τ_i vs. τ_{int} for fixed beam diameters ranging from 80 μm to 500 μm. For fixed beam diameter, as scan speed increases, τ_{int} decreases and τ_i decreases as well. This results from the fact that as scan speed increases for fixed beam diameter, beam–material interaction time τ decreases and the heat flux input rate $\dot{q}$ increases. However, examining various constant diameter plots for fixed τ_{int} in Fig. 1(a), we observe that τ_i increases with increasing beam diameter. This is also a result of the decrease in the heat flux input rate for fixed τ_{int} in addition to decreasing heat flux input as beam diameter increases. The slope of τ_i vs. τ_{int} is an increasing function of beam diameter. This results from the changing rate of heat flux input rate as a function of beam diameter.

Fig. 1(b) shows plots of τ_i vs. ϕ for fixed scan speeds ranging from 0.5 to 1.25 m/s, revealing that for fixed scan speeds, τ_i decreases as ϕ increases. In this case as well, heat flux input and heat flux input rate increase. Therefore, $\dot{q}$, the heat flux input rate can be regarded as the dominant factor influencing τ_i.

4.1.2. Time to initiate vaporization

Fig. 1(c) shows τ_{vi} as a function of τ_{int} for fixed beam diameters, revealing that for fixed beam diameter, τ_{vi} increases as τ_{int} increases. For fixed beam diameter, as scan speed increases, beam–material interaction time τ decreases and the heat flux input rate increases. However, some cases for the diameter larger than 350 μm and all the cases for the diameter larger than 450 μm do not exhibit vaporization. This result indicates that a minimum supplied total energy density is needed to initiate vaporization. We observe that τ_{vi} increases with increasing beam diameter for fixed τ_{int} in Fig. 1(c). This is a result of the decrease in heat flux input rate for fixed

Table 1
Parameters used for numerical computations I

Diameter (μm)	80	100	150	200	250	300	350	400	450	500
Scan speed (m/s)	1.0	1.0	0.5	0.5	0.5	0.5	0.5	0.5	0.5	0.5
	2.5	2.5	0.75	0.75	0.75	0.75	0.75	0.75	0.75	0.75
	5.0	5.0	1.0	1.0	1.0	1.0	1.0	1.0	1.0	1.0
	7.5	7.5	1.25	1.25	1.25	1.25	1.25	1.25	1.25	1.25

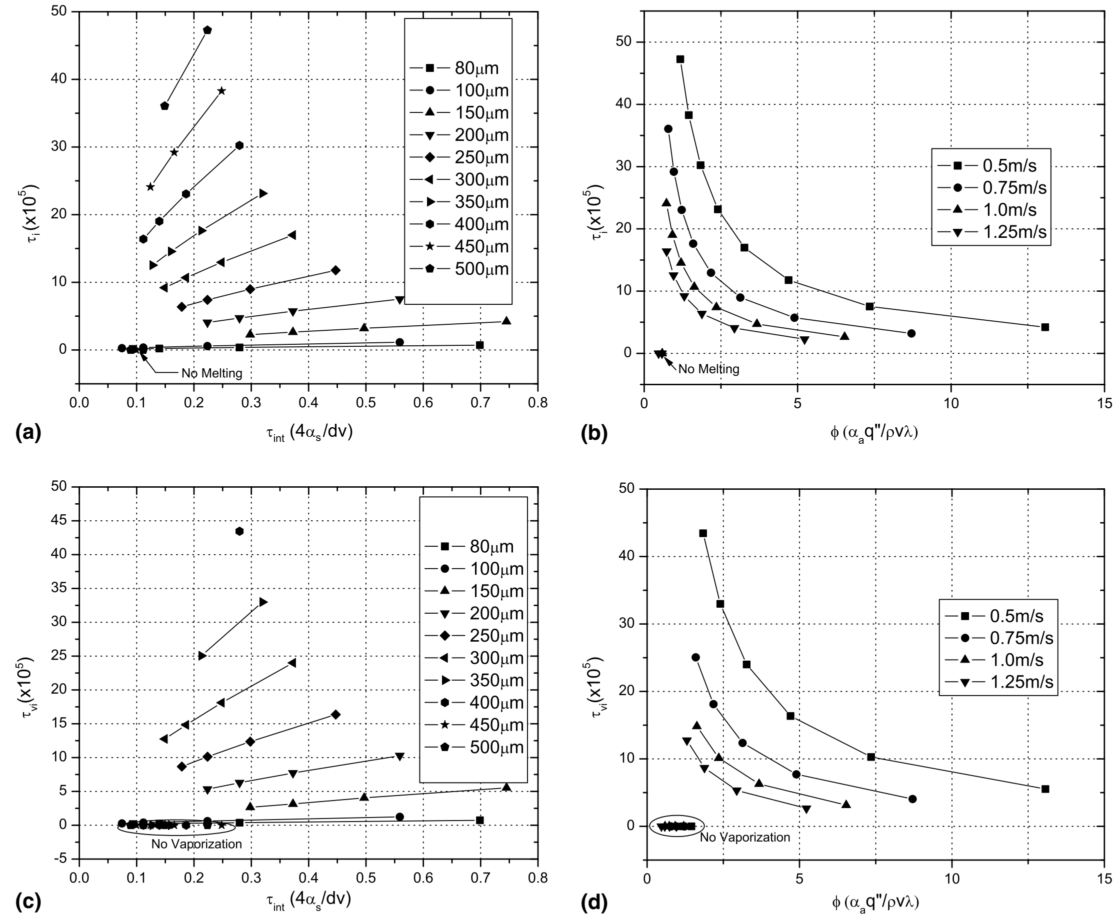

Fig. 1. (a) Dimensionless time to initiate melting vs. dimensionless beam material interaction time at fixed beam diameters. (b) Dimensionless time to initiate melting vs. dimensionless energy density at fixed scan speeds. (c) Dimensionless time to initiate vaporization vs. dimensionless beam–material interaction time at fixed beam diameters. (d) Dimensionless time to initiate vaporization vs. dimensionless energy density at fixed scan speeds.

τ_{int} as beam diameter increases. The slope of τ_{vi} vs. τ_{int} is an increasing function of beam diameter in a manner similar to τ_i vs. τ_{int}.

Fig. 1(d) shows τ_{vi} as a function of ϕ for fixed scan speeds. For fixed scan speeds, τ_{vi} decreases as ϕ increases (beam diameter decreases). This results from the increase of the heat flux input rate. Therefore, the heat flux input rate is dominant factor controlling τ_{vi}.

4.1.3. Time to reach maximum melting depth

Fig. 2(a) shows τ_{max} as a function of τ_{int} for fixed beam diameters. For each fixed beam diameter, as scan speed increases, smaller beam–material interaction time τ causes both τ_{int} and τ_{max} to decrease. From Fig. 2(a) it is observed that for fixed τ_{int}, τ_{max} increases with increasing beam diameter due to the fact that although the heat flux input rate decreases and supplied total energy density Q_r $(= \frac{2P}{\pi dv})$ remains constant, beam–material interaction time τ increases as beam diameter increases for fixed τ_{int}. Fig. 2(b) shows τ_{max} as a function of ϕ for fixed scan speeds. For each fixed scan speed, as beam diameter increases (and therefore ϕ decreases), τ_{max} increases due to increasing beam–material interaction time. In other words, τ_{max} is dominated by τ, the beam–material interaction time.

4.1.4. Time for melting and resolidification

Fig. 2(c) shows plot of τ_{tot} vs. τ_{int} for fixed beam diameters. For each fixed beam diameter, as scan speed increases, both τ_{int} and τ_{tot} decrease. This results from the fact that both beam–material interaction time and supplied total energy density decrease as a result of increasing scan speed. For fixed τ_{int}, as beam diameter increases, τ_{tot} increases due to increasing beam–material interaction time although the supplied total energy density remains constant. Fig. 2(d) shows plot of τ_{tot} vs.

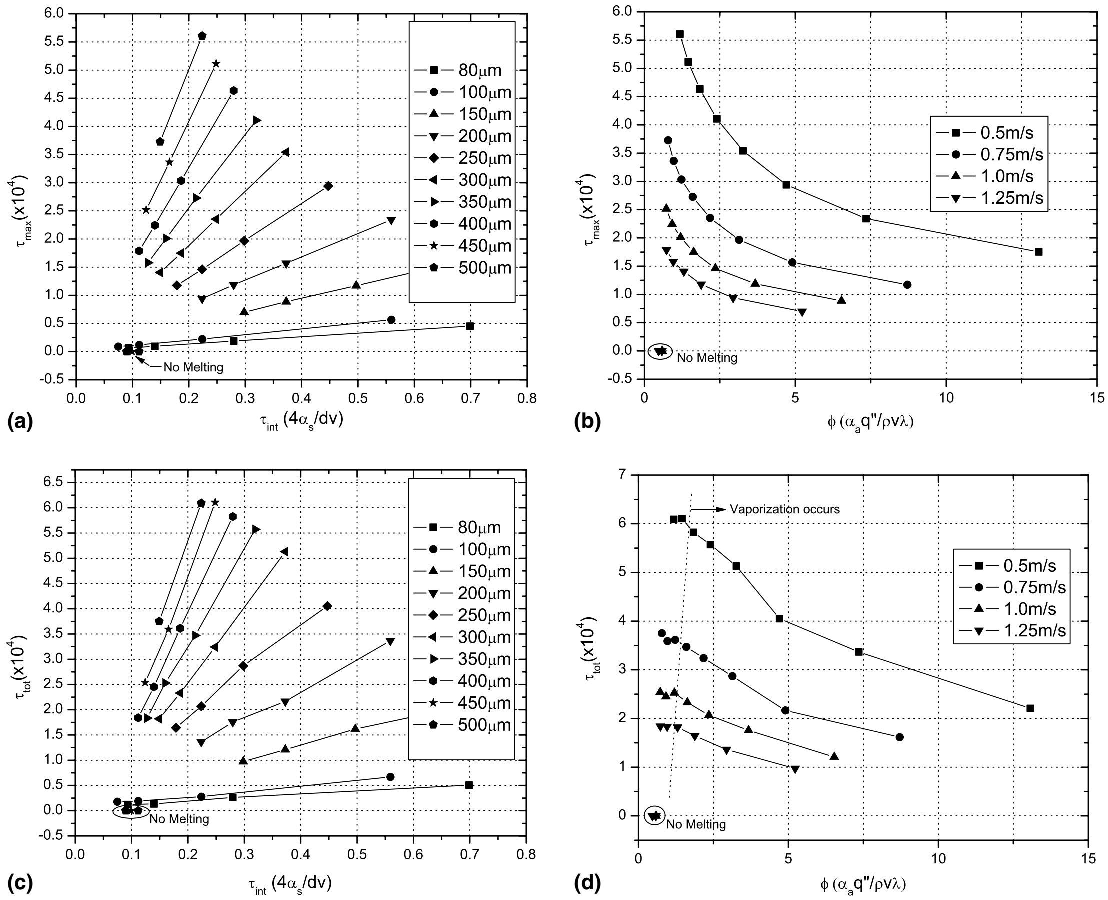

Fig. 2. (a) Dimensionless time to reach maximum melting depth vs. dimensionless beam–material interaction time at fixed beam diameters. (b) Dimensionless time to reach maximum melting depth vs. dimensionless energy density at fixed scan speeds. (c) Dimensionless time for melting and resolidification vs. dimensionless beam–material interaction time at fixed beam diameters. (d) Dimensionless time for melting and resolidification vs. dimensionless energy density at fixed scan speeds.

ϕ for fixed scan speeds. The dotted line separates those cases where no vaporization occurs and those in which there is some vaporization. When no vaporization occurs, τ_{tot} is a decreasing function of ϕ to a minimum due to decreasing beam–material interaction time and after the minimum, τ_{tot} is an increasing function of ϕ due to increasing supplied total energy density. However, when vaporization occurs, some material is ablated and this affects τ_{tot}. In such cases, the influence of ϕ is reversed. In other words, for cases with vaporization, at fixed scan speed, τ_{tot} decreases with increasing ϕ. Therefore, the onset of vaporization reverses τ_{tot} from an increasing function of ϕ to a decreasing one.

4.1.5. Maximum melting depth

Fig. 3(a) and (b) show plots of ζ_{max} vs. τ_{int} for fixed beam diameters and ζ_{max} vs. ϕ for fixed scan speeds respectively. Fig. 3(a) shows that for each fixed beam diameter, as scan speed increases, both τ_{int} and ζ_{max} decrease. This results from the fact that as scan speed increases for each fixed beam diameter, the supplied total energy density decreases. The slope of ζ_{max} vs. τ_{int} is an increasing function of beam diameter and it shows a distinct difference between 300 μm and 350 μm. Fig. 3(b) shows that for fixed scan speed, ζ_{max} increases with increasing ϕ (decreasing beam diameter). As ϕ increases for fixed scan speed, the supplied total energy density increases. Therefore, ζ_{max} can be regarded as a function of supplied total energy density. The dotted line in Fig. 3(b) separates those cases where no vaporization occurs and those in which there is some vaporization. For each fixed scan speed, a steep gradient for ζ_{max} vs. ϕ in the absence of vaporization is smoothened with the onset of vaporization.

4.1.6. Maximum vaporization depth

Fig. 3(c) shows $\zeta_{v,max}$ as a function of τ_{int} for fixed beam diameters. As τ_{int} increases for each fixed beam

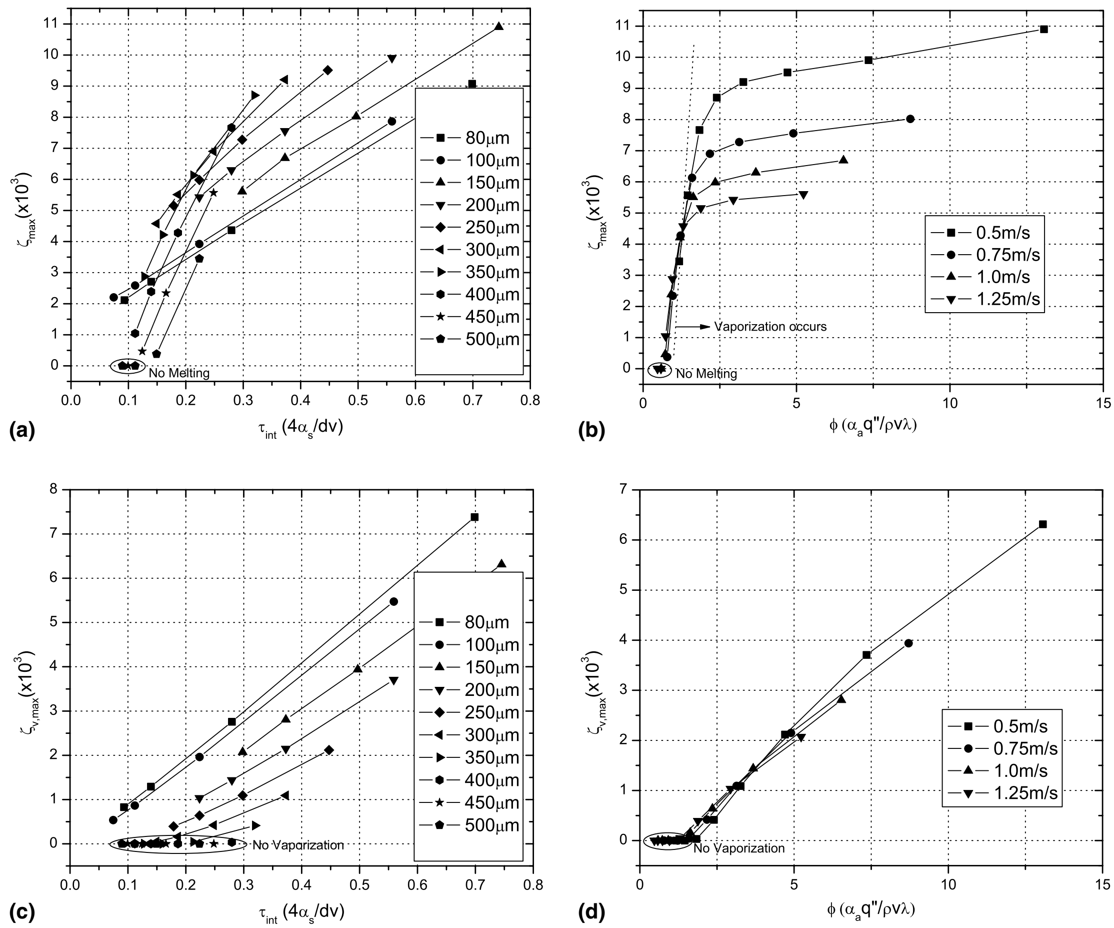

Fig. 3. (a) Dimensionless maximum melting depth vs. dimensionless beam–material interaction time at fixed beam diameters. (b) Dimensionless maximum melting depth vs. dimensionless energy density at fixed scan speeds. (c) Dimensionless maximum vaporization depth vs. dimensionless beam–material interaction time at fixed beam diameters. (d) Dimensionless maximum vaporization depth vs. dimensionless energy density at fixed scan speeds.

diameter, $\zeta_{v,max}$ increases due to increasing supplied total energy density. The slope of $\zeta_{v,max}$ vs. τ_{int} is a weakly decreasing function of beam diameter. Fig. 3(d) shows $\zeta_{v,max}$ as a function of ϕ for fixed scan speeds. As ϕ increases for each fixed scan speed, $\zeta_{v,max}$ also increases due to increasing supplied total energy density. The slope of $\zeta_{v,max}$ vs. ϕ is a weakly decreasing function of scan speed. Therefore, the supplied total energy density is a dominant factor controlling $\zeta_{v,max}$.

4.1.7. Initial substrate temperature and surface temperature

Fig. 4(a) shows ζ_{max} as a function of different initial substrate temperatures. As substrate temperature increases, ζ_{max} increases as expected since lesser laser energy is needed to raise the temperature to the melting point and consequently the melt interface penetrates deeper. Similarly, we derived scaling laws for τ_i, τ_{vi}, τ_{max}, τ_{tot} and $\zeta_{v,max}$ as well as ζ_{max} as a function of dimensionless initial substrate temperature θ_i. The equations for these scaling laws are shown in Table 3. τ_i and τ_{vi} are decreasing functions of θ_i, while τ_{max}, τ_{tot}, ζ_{max} and $\zeta_{v,max}$ are increasing ones as expected.

Fig. 4(b) shows the numerical solution and approximate closed form solution of surface temperature for three different cases. When there is no melting or vaporization, both solutions are nearly identical. This implies that the radiative losses accounted for in our numerical solution but neglected in Prokhorov's closed form solution are negligible in comparison with heat conduction into the metal bulk. When there is melting without vaporization, our numerical solution estimates a higher peak surface temperature when compared to Prokhorov's closed form solution [5]. This result can be attributed to two probable causes. First, our model includes vaporization while Prokhorov's does not. Second, our model incorporates the appropriate thermal diffu-

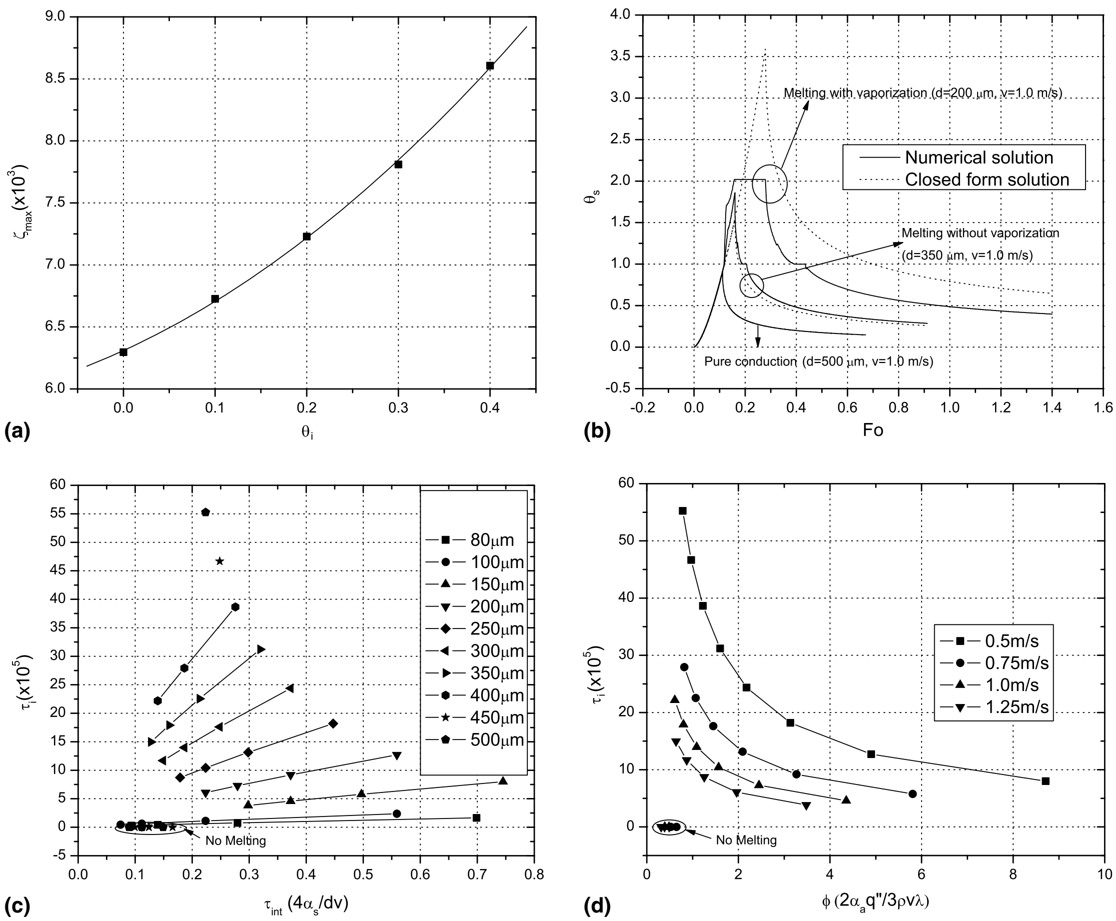

Fig. 4. (a) Dimensionless maximum melting depth vs. dimensionless initial substrate temperature ($d = 200$ μm, $v = 1.0$ m/s). (b) Dimensionless surface temperature vs. Fourier number. (c) Dimensionless time to initiate melting vs. dimensionless beam–material interaction time at fixed beam diameters. (d) Dimensionless time to initiate melting vs. dimensionless energy density at fixed scan speeds.

Table 3
Equation of scaling laws in ramp heat flux input ($d = 200$ μm, $v = 1$ m/s)

	Equations ($\theta_i = \frac{T_i - T_\infty}{T_m - T_\infty}$)
$\tau_i(\frac{\alpha t}{L_2}) \times 10^5$	$4.719 - 3.147\theta_i - 0.731\theta_i^2$
$\tau_{vi}(\frac{\alpha t}{L_2}) \times 10^5$	$6.282 - 2.076\theta_i - 0.311\theta_i^2$
$\tau_{max}(\frac{\alpha t}{L_2}) \times 10^4$	$1.193 - 0.087\theta_i + 0.976\theta_i^2$
$\tau_{tot}(\frac{\alpha t}{L_2}) \times 10^4$	$1.773 + 0.408\theta_i + 5.995\theta_i^2$
$\zeta_{max}(\frac{x}{L}) \times 10^3$	$6.31 + 3.38\theta_i + 5.80\theta_i^2$
$\zeta_{v,max}(\frac{x}{L}) \times 10^3$	$1.44 + 0.881\theta_i + 0.072\theta_i^2$

sivities for Nickel in the solid and liquid states while Prokhorov assumes a constant diffusivity corresponding to the solid state. Note that the thermal diffusivity of liquid Nickel is lower than that of solid Nickel. When there is melting accompanied by vaporization, Prokhorov's closed form solution estimates a higher peak surface temperature compared to our numerical solution. This difference reflects the effect of the latent heat of evaporation accounted for in our numerical solution but neglected in Prokhorov's closed form approximate solution, which has also been reported elsewhere [1]. The peak temperature from Prokhorov's solution is far in excess of the melt temperatures as was observed for a step heat flux input [2]. This is likely a result of not including of latent heat of vaporization. It should also be noted that for a linear ramp heat flux input, the materials remain molten for a time shorter than the molten residence time for step heat flux input [2]. This results from the fact that for the same combination of beam diameter and scan speed, the supplied total energy density for step heat flux input ($Q_s = \frac{4P}{\pi dv}$) is twice that for linear ramp heat flux input ($Q_r = \frac{2P}{\pi dv}$).

4.2. Quadratic heat flux input

4.2.1. Time to initiate melting

Fig. 4(c) shows plot of τ_i vs. τ_{int} for fixed beam diameters. For each fixed beam diameter, as scan speed increases, both τ_{int} and τ_i decrease. Although beam–material interaction time and supplied total energy density Q_q $(=\frac{4P}{3\pi dv})$ decrease with increasing scan speed for fixed beam diameter, the heat flux input rate $\dot{q}$ increases. The slope of τ_i vs. τ_{int} is an increasing function of beam diameter. Fig. 4(c) shows that for fixed τ_{int}, as beam diameter increases, τ_i increases due to the decreasing heat flux input rate. From Fig. 4(d) it is observed that for fixed ϕ, τ_i is inversely proportional to the heat flux input rate. These results imply that τ_i can be regarded as primarily a function of $\dot{q}$, the heat flux input rate.

4.2.2. Time to initiate vaporization

Fig. 5(a) shows τ_{vi} as a function of τ_{int} for fixed beam diameters. For each fixed beam diameter, as τ_{int} increases (scan speed decreases), τ_{vi} increases in spite of increased beam–material interaction time and increased supplied total energy density. As scan speed decreases for fixed beam diameter, $\dot{q}$, the heat flux input rate decreases. The slope of τ_{vi} vs. τ_{int} is an increasing function of beam diameter. Therefore, the heat flux input rate can be also regarded as the dominant factor controlling τ_{vi}.

4.2.3. Time to reach maximum melting depth

Fig. 5(b) and (c) show plots of τ_{max} vs. τ_{int} for fixed beam diameters and τ_{max} vs. ϕ for fixed scan speeds respectively. Fig. 5(b) shows that for each fixed beam diameter, as scan speed increases, τ_{max} decreases due to decreasing beam–material interaction time. For fixed

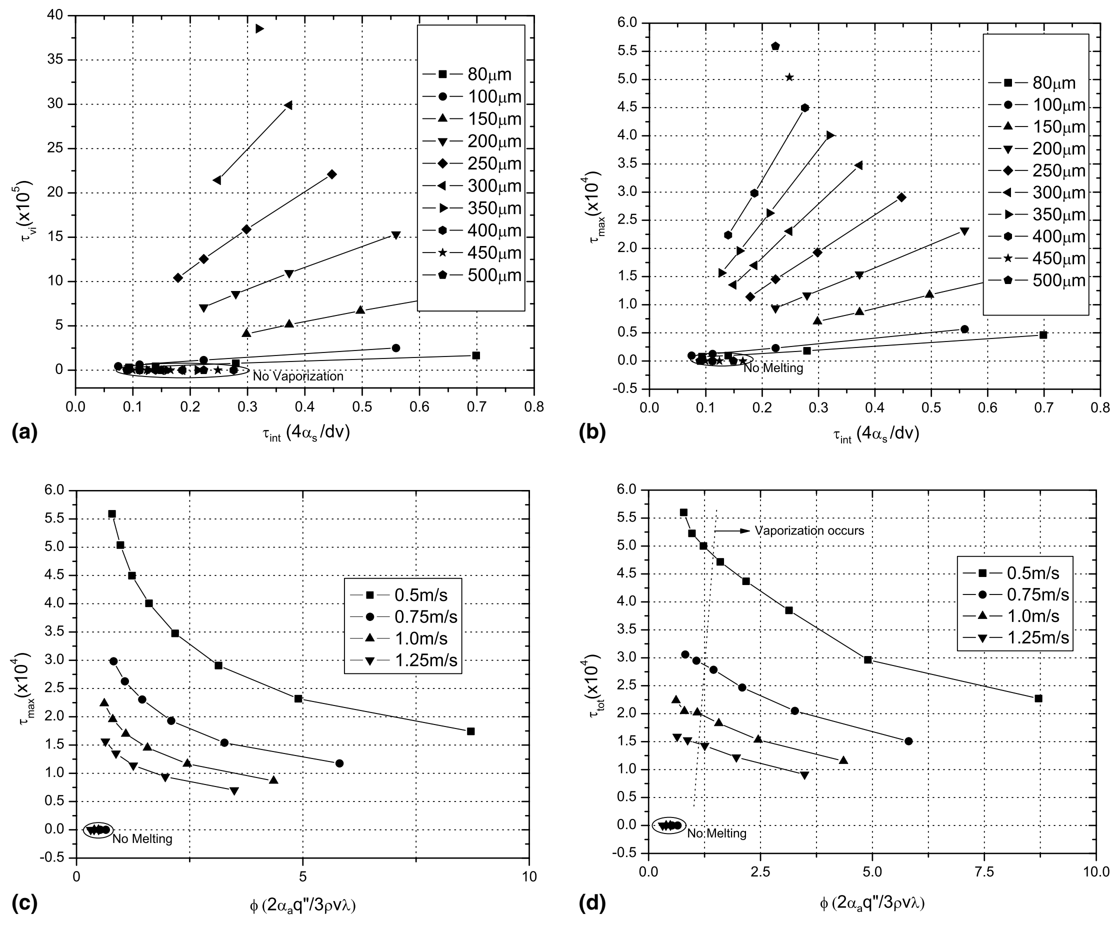

Fig. 5. (a) Dimensionless time to initiate vaporization vs. dimensionless beam–material interaction time at fixed beam diameters. (b) Dimensionless time to reach maximum melting depth vs. dimensionless beam–material interaction time at fixed beam diameters. (c) Dimensionless time to reach maximum melting depth vs. dimensionless energy density at fixed scan speeds. (d) Dimensionless time for melting and resolidification vs. dimensionless energy density at fixed scan speeds.

τ_{int}, as the beam diameter increases, τ_{max} increases due to increasing beam–material interaction time in spite of constant supplied total energy density. Fig. 5(c) shows that for each fixed scan speed, as ϕ increases (beam diameter decreases), τ_{max} decreases due to decreasing beam–material interaction time. These results imply that τ_{max} is primarily a function of beam–material interaction time.

4.2.4. Time for melting and resolidification

Fig. 5(d) shows τ_{tot} vs. ϕ for fixed scan speeds. The dotted line separates those cases where no vaporization occurs and those in which there is some vaporization. When no vaporization occurs, τ_{tot} decreases with increasing ϕ. For fixed scan speeds, as ϕ increases (beam diameter decreases), supplied total energy density increases (owing to the inverse square dependence of q'' on diameter) but the beam–material interaction time decreases. This implies that dominant factor influencing τ_{tot} in the absence of vaporization is the beam–material interaction time. When vaporization occurs, some material is ablated and this affects τ_{tot}. For cases involving vaporization, at fixed scan speed, τ_{tot} decreases with increasing ϕ due to decreasing beam–material interaction time and ablation of material.

4.2.5. Maximum melting depth

Fig. 6(a) shows plot of ζ_{max} vs. τ_{int} for fixed beam diameters. For each fixed beam diameter, as scan speed increases, τ_{int} decreases and ζ_{max} decreases due to decreasing supplied total energy density. The slope of ζ_{max} vs. τ_{int} is an increasing function of beam diameter.

Fig. 6(b) shows plot of ζ_{max} vs. ϕ for fixed scan speeds. The dotted line separates those cases where no vaporization occurs and those in which there is some vaporization. For fixed scan speed, ζ_{max} increases with

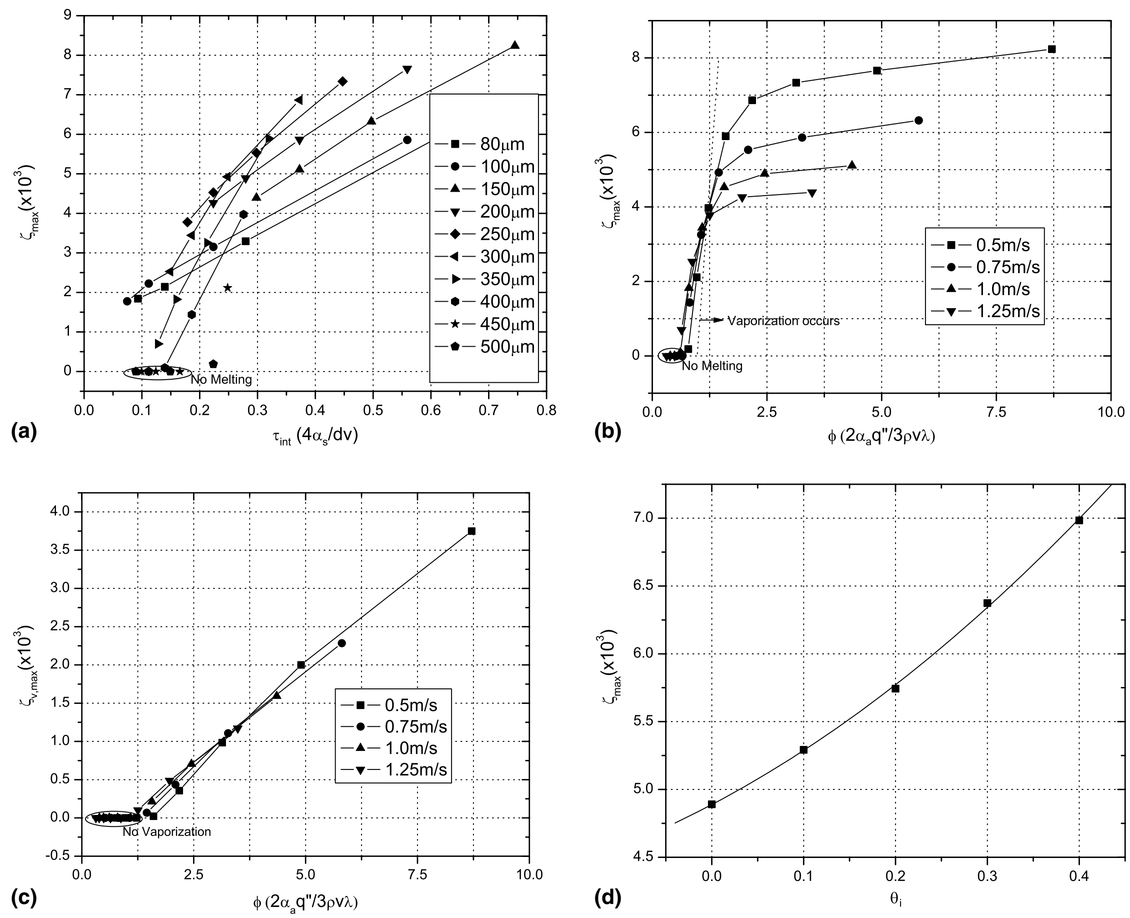

Fig. 6. (a) Dimensionless maximum melting depth vs. dimensionless beam–material interaction time at fixed beam diameters. (b) Dimensionless maximum melting depth vs. dimensionless energy density at fixed scan speeds. (c) Dimensionless maximum vaporization depth vs. dimensionless energy density at fixed scan speeds. (d) Dimensionless maximum melting depth vs. dimensionless initial substrate temperature ($d = 200$ μm, $v = 1.0$ m/s).

increasing ϕ (decreasing beam diameter) due to increasing supplied total energy density. For each fixed scan speed, a steep gradient for ζ_{max} vs. ϕ in the absence of vaporization is smoothened with the onset of vaporization. Therefore, ζ_{max} can be regarded as a function of supplied total energy density.

4.2.6. Maximum vaporization depth

Fig. 6(c) shows $\zeta_{v,max}$ as a function of ϕ for fixed scan speeds. As ϕ increases for each fixed scan speed, $\zeta_{v,max}$ increases due to increasing supplied total energy density. The slope of $\zeta_{v,max}$ vs. ϕ is a weakly decreasing function of scan speed. Therefore, $\zeta_{v,max}$ can be also regarded as a function of supplied total energy density.

4.2.7. Initial substrate temperature and surface temperature

Fig. 6(d) shows ζ_{max} as a function of different initial substrate temperatures. As substrate temperature increases, ζ_{max} increases as expected since lesser laser energy needs to be supplied to raise the temperature to melting point and consequently the melt interface penetrates deeper. Similarly, we derive scaling laws for τ_i, τ_{vi}, τ_{max}, τ_{tot} and $\zeta_{v,max}$ as well as ζ_{max} as a function of dimensionless substrate temperatures. The equations for these scaling laws are shown in Table 4. τ_i and τ_{vi} are decreasing functions of θ_i, while τ_{max}, τ_{tot}, ζ_{max} and $\zeta_{v,max}$ are increasing ones as expected.

Fig. 7 shows the numerical solution and approximate closed form solution of surface temperature distribution for three different cases. When there is no melting or vaporization, both solutions are nearly identical. This implies that the radiative losses accounted for in our numerical solution but neglected in Prokhorov's closed form solution are negligible in comparison with heat conduction into the metal bulk, as is observed in the case of linear ramp heat flux input. However, when there is melting without vaporization, our numerical solution estimates a higher peak surface temperature compared to Prokhorov's closed form solution [5]. This result can be attributed to two probable causes. First, our model includes vaporization while Prokhorov's does not. Second, our model incorporates the appropriate thermal diffusivities for Nickel in the solid and liquid states while Prokhorov assumes a constant diffusivity corresponding to the solid state. Note that the thermal diffusivity of liquid Nickel is lower than that of solid Nickel. On the other hand, when there is melting accompanied by vaporization, Prokhorov's closed form solution estimates a higher peak surface temperature compared to our numerical solution. This difference reflects the effect of the latent heat of evaporation accounted for in our numerical solution but neglected in Prokhorov's closed form solution. The peak temperature from Prokhorov's solution is far in excess of the melt temperatures as was observed for a linear ramp heat flux input. This is likely a result of not including of latent heat of vaporization. It should also be noted that for a quadratic heat flux input, the materials remain molten for a time shorter than the molten residence time for a linear ramp heat flux input. This results from the fact that for the same combination of beam diameter and scan speed, the supplied total energy density for linear ramp heat flux input ($Q_r = \frac{2P}{\pi dv}$) is 1.5 times that for quadratic heat flux input ($Q_q = \frac{4P}{3\pi dv}$).

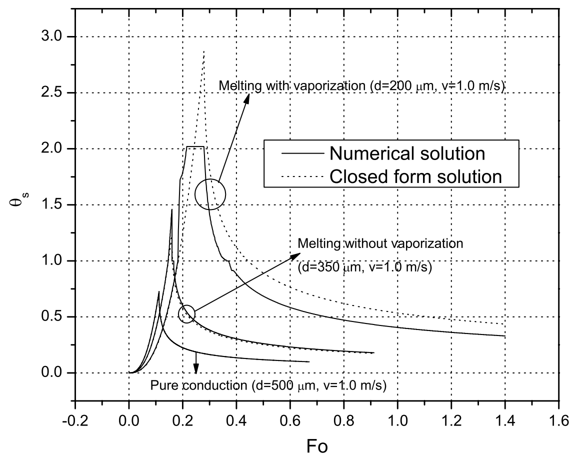

Fig. 7. Dimensionless surface temperature vs. Fourier number.

Table 4
Equation of scaling laws in quadratic heat flux input ($d = 200$ μm, $v = 1$ m/s)

	Equations ($\theta_i = \frac{T_i - T_\infty}{T_m - T_\infty}$)
$\tau_i(\frac{\alpha t}{L_2}) \times 10^5$	$7.281 - 2.863\theta_i - 1.294\theta_i^2$
$\tau_{vi}(\frac{\alpha t}{L_2}) \times 10^5$	$8.605 - 1.543\theta_i - 0.511\theta_i^2$
$\tau_{max}(\frac{\alpha t}{L_2}) \times 10^4$	$1.166 + 0.023\theta_i + 0.601\theta_i^2$
$\tau_{tot}(\frac{\alpha t}{L_2}) \times 10^4$	$1.537 + 0.412\theta_i + 3.389\theta_i^2$
$\zeta_{max}(\frac{x}{L}) \times 10^3$	$4.890 + 3.570\theta_i + 4.260\theta_i^2$
$\zeta_{v,max}(\frac{x}{L}) \times 10^4$	$7.059 + 5.754\theta_i + 1.991\theta_i^2$

5. Summary and conclusions

A dimensionless analysis of the controlling parameters under various conditions including different beam diameters, scan speeds, and substrate temperatures was conducted for ramp and quadratic heat flux inputs. Characteristics of dimensionless time to initiate melting, time to initiate vaporization, time to reach the maximum melting depth, total time for melting and resolidification, dimensionless maximum melting depth and maximum vaporization depth were obtained under ramp and quadratic heat flux input from the results of this preliminary model. A summary of our findings is presented in Tables 5 and 6. For both ramp and quadratic heat

Table 5
Summary table for linear ramp heat flux input

Process variable	Dominant control parameter
τ_i	$\dot{q}$
τ_{vi}	$\dot{q}$
τ_{max}	τ
τ_{tot}	Q_r, τ (without vaporization)
	$x_{vf,max}$ (with vaporization)
ζ_{max}	Q_r
$\zeta_{v,max}$	Q_r

Table 6
Summary table for quadratic heat flux input

Process variable	Dominant control parameter
τ_i	$\dot{q}$
τ_{vi}	$\dot{q}$
τ_{max}	τ
τ_{tot}	τ (without vaporization)
	$x_{vf,max}$ (with vaporization)
ζ_{max}	Q_q
$\zeta_{v,max}$	Q_q

flux input, τ_i and τ_{vi} are inversely proportional to the heat flux input rate. τ_{max} is a function of beam–material interaction time and when no vaporization occurs, τ_{tot} is related with supplied total energy density and beam–material interaction time for ramp heat flux input and can be regarded as a function of beam–material interaction time for quadratic heat flux input. However, when vaporization occurs, some material is ablated and this affects τ_{tot}. ζ_{max} and $\zeta_{v,max}$ can be regarded as a function of supplied total energy density. We also derived scaling laws for τ_i, τ_{vi}, τ_{max}, τ_{tot}, ζ_{max} and $\zeta_{v,max}$ as a function of dimensionless substrate temperatures for each type of heat flux input. This understanding is helpful to implement effective process control in direct selective laser sintering of metals with knowledge of the results for step heat flux input given in a previous article [2].

Acknowledgements

This work was supported by National Science Foundation Grant DMI 0115205.

References

[1] E.M. Breinan, B.H. Kear, Rapid solidification laser processing at high power density, in: M. Bass (Ed.), Laser Materials Processing, North-Holland Publishing Company, 1983, pp. 235–295.
[2] H. Chung, S. Das, Numerical modeling of scanning laser-induced melting, vaporization and resolidification in metals subjected to step heat flux input, Int. J. Heat Mass Transfer, in press. doi:10.1016/j.ijheatmasstransfer.2004.05.003.
[3] S. Das, Direct Selective Laser Sintering of High Performance Metals–Machine Design, Process Development and Process Control, Ph.D. Thesis, University of Texas, Austin, TX, 1998.
[4] S.V. Patankar, Numerical Heat Transfer and Fluid Flow, Taylor and Francis, 1980.
[5] A.M. Prokhorov, V.I. Konov, I. Ursu, I.N. Mihailescu, Laser Heating of Metals, Adam Hilger, 1990.